

MS-ISSM: Objective Quality Assessment of Point Clouds Using Multi-scale Implicit Structural Similarity

Zhang Chen, Shuai Wan, *Member, IEEE*, Yuezhe Zhang, Siyu Ren, Fuzheng Yang, *Member, IEEE*, and Junhui Hou, *Senior Member, IEEE*

Abstract—The unstructured and irregular nature of points poses a significant challenge for accurate point cloud quality assessment (PCQA), particularly in establishing accurate perceptual feature correspondence. To tackle this, we propose the Multi-scale Implicit Structural Similarity Measurement (MS-ISSM). Unlike traditional point-to-point matching, MS-ISSM utilizes radial basis function (RBF) to represent local features continuously, transforming distortion measurement into a comparison of implicit function coefficients. This approach effectively circumvents matching errors inherent in irregular data. Additionally, we propose a ResGrouped-MLP quality assessment network, which robustly maps multi-scale feature differences to perceptual scores. The network architecture departs from traditional flat multi-layer perceptron (MLP) by adopting a grouped encoding strategy integrated with residual blocks and channel-wise attention mechanisms. This hierarchical design allows the model to preserve the distinct physical semantics of luma, chroma, and geometry while adaptively focusing on the most salient distortion features across High, Medium, and Low scales. Experimental results on multiple benchmarks demonstrate that MS-ISSM outperforms state-of-the-art metrics in both reliability and generalization. The source code is available at: <https://github.com/ZhangChen2022/MS-ISSM>.

Index Terms—point cloud, quality assessment, multi-scale, implicit representation, multi-layer perceptron

I. INTRODUCTION

PPOINT clouds are fundamental to 3D representation in applications ranging from autonomous driving to augmented and virtual reality (AR/VR) [1], [2]. However, their irregular and unstructured nature makes accurate quality assessment challenging, especially given distortions from noise, downsampling, and compression [3]. While subjective assessment provides reliable ground truth, it is costly and time-consuming,

Zhang Chen and Yuezhe Zhang are with the School of Electronics and Information, Northwestern Polytechnical University, Xi'an 710129, China (e-mail: chen-zhang@mail.nwpu.edu.cn; yuezhe.zhang@mail.nwpu.edu.cn).

Shuai Wan is with the School of Electronics and Information, Northwestern Polytechnical University, Xi'an 710129, China, and also with the School of Engineering, Royal Melbourne Institute of Technology, Melbourne, VIC 3001, Australia (e-mail: swan@nwpu.edu.cn).

Siyu Ren and Junhui Hou are with the Department of Computer Science, City University of Hong Kong, Hong Kong SAR (e-mail: siyuren2-c@my.cityu.edu.hk; jh.hou@cityu.edu.hk).

Fuzheng Yang is with the School of Telecommunication Engineering, Xidian University, Xi'an 710071, China (e-mail: fzhyang@mail.xidian.edu.cn).

This work was supported in part by the TCL Science and Technology Innovation Fund, in part by the NSFC Fund 62371358, in part by the NSFC Excellent Young Scientists Fund 62422118 and in part by the Hong Kong Research Grants Council under Grants 11219422 and 11219324.

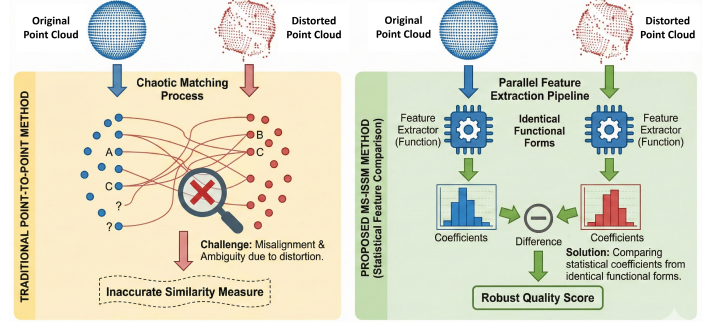


Fig. 1. The difference between the MS-ISSM and the traditional point-to-point method.

necessitating efficient objective metrics that correlate well with human perception [4]–[6].

Existing objective point cloud quality assessment (PCQA) methods generally fall into two categories: projection-based and point-based [7]. Projection-based methods project 3D data onto 2D planes, leveraging mature image quality assessment (IQA) algorithms [8]–[11]. However, this dimensionality reduction often causes geometry loss and introduces viewpoint dependency [12]. Conversely, point-based methods directly utilize 3D spatial features [13], [14]. A common approach involves identifying point-to-point correspondences via nearest-neighbor search to compute geometry or attribute distortions, which introduces two main limitations. First, the unstructured nature of point clouds makes accurate correspondence difficult. Distortions like downsampling or noises often change the density and spatial distribution of points, leading to matching misalignment and calculation errors. Second, there is a discrepancy between discrete point-to-point errors and actual human visual perception. Traditional point-based metrics evaluate localized differences in isolation and fail to capture continuous structural changes on the surface. Consequently, different distortion types can yield similar point-to-point error values but exhibit varying perceptual degradation to the human visual system (HVS) [15], [16].

To address these limitations, we propose the multi-scale implicit structural similarity method (MS-ISSM). Building upon our previous work utilizing radial basis function (RBF) interpolation [17], we represent point cloud features as continuous implicit functions rather than discrete points. As shown in Fig. 1, MS-ISSM models local spatial features as implicit

functions and measures distortion by comparing their function coefficients. This approach bypasses the error-prone point matching process by evaluating localized structural topologies as a whole. Moreover, differences in coefficients can reflect the continuous surface variations and structural degradation. Finally, to handle complex non-linear mappings, we integrate a multi-scale feature extraction strategy and propose a ResGrouped-MLP regression network to map these multi-scale coefficient differences to subjective quality scores. The main contributions of this paper are summarized as follows:

- We propose representing point cloud features using RBF implicit functions. By converting discrete point-based feature differences into implicit function coefficient differences, we mitigate the accumulation of matching errors caused by the irregular nature of point clouds.
- We design a ResGrouped-MLP quality assessment network. It incorporates a Log-Modulus transformation to handle heavy-tailed feature distributions and integrates residual blocks with channel-wise attention to adaptively weight physical semantics (luma, chroma, geometry) across multiple scales.
- Extensive experiments in public datasets demonstrate that MS-ISSM achieves competitive performance in both reliability and generalization compared to the state-of-the-art PCQA metrics.

The remainder of this paper is organized as follows: Section II reviews related work. Section III details the problem formulation and theoretical foundation. Section IV describes the proposed MS-ISSM. Section V presents experimental results, and Section VI concludes the paper.

II. RELATED WORK

This section reviews existing PCQA methods, categorized into single-scale and multi-scale approaches.

a) *Single-scale PCQA Methods*: Single-scale methods quantify distortion by measuring geometric or attribute variations between corresponding points. Standard metrics rely on point-to-point Euclidean distances or feature differences, widely adopted in compression standards [7]. Enhancements to these metrics include measuring projection distance along normal directions [13], utilizing Mahalanobis distance to capture spatial distribution [18], or calculating point-to-grid distances [19]. To improve perceptual correlation, other approaches focus on feature disparities, such as angular differences between normal vectors [20] or curvature variations [21]. While these algorithms possess low computational complexity [22], they often fail to align with human visual perception due to the lack of perceptual modeling.

b) *Multi-scale PCQA Methods*: To better approximate human perception, researchers have integrated multi-scale and joint features. Meynet et al. proposed the Point Cloud Quality Metric (PCQM) [14], [23], a linear combination of curvature, chroma, and brightness. Other hand-crafted feature methods combine geometric statistics with local plane features [24], utilize gradients from local graphs [25], [26], analyze geometric topology alongside color distribution [27], or measure multi-scale spatial potential energy [28], transformational complexity [29] and perception-guided hybrid metrics (PHM) [30].

Additionally, Lazzarotto et al. developed MS-PointSSIM by weighting structural similarity across spatial scales [31].

Recent advancements leverage learning-based frameworks. These include CNN-based mapping of feature differences [32], and GNNs for learning local intrinsic dependencies [33]. Other works employ PCA on local neighborhoods [34] or integrate spherical graph wavelet (SGW) coefficients with support vector regression (FRSVR) [35], [36]. Similarly, Cui et al. combined projected structural similarity with wavelet sub-band features in a learning framework [37]. Wang et al. also explored joint assessment using multi-scale texture features from 2D images and 3D points [38].

Alternatively, projection-based methods evaluate quality by rendering point clouds into 2D images and applying image quality assessment (IQA) models [39]–[41]. However, projection alters 3D characteristics, leading to the loss of geometric details such as depth and occlusion relationships. Furthermore, while point-based learning methods show promise, they struggle with the fundamental challenge of establishing accurate point correspondences for distorted data.

III. PROBLEM FORMULATION

A. Points Correspondence and Perceptual Distortion Measurement

A point cloud is defined as a set of geometric coordinates and associated attributes. Let the original point cloud \mathbf{P}^O and the distorted point cloud \mathbf{P}^D be represented as:

$$\mathbf{P}^\alpha = \{\mathbf{p}_n^\alpha, \mathbf{q}_n^\alpha\}_{n=1}^{N_\alpha}, \quad (1)$$

where $\alpha \in \{O, D\}$ denotes the type of point clouds, and N_α is the number of points. Each element consists of geometric coordinates \mathbf{p}_n^α and attributes \mathbf{q}_n^α . Ideally, the perceptual distortion $D(\mathbf{P}^O, \mathbf{P}^D)$ is measured by finding a feature bijection ψ that minimizes the feature difference:

$$D(\mathbf{P}^O, \mathbf{P}^D) = \min_{\psi: \mathbf{P}^O \rightarrow \mathbf{P}^D} \left\{ \frac{1}{N_\psi} \sum_{\mathbf{p}_i^O \in \mathbf{P}^O} \left\| M_O(\mathbf{p}_i^O) - M_D(\psi(\mathbf{p}_i^O)) \right\|_2 \right\}, \quad (2)$$

where $M_\alpha(\cdot)$ extracts features (e.g., geometry, color). However, since N_O often differs from N_D , a strict bijection is impractical. Consequently, classical methods approximate this using nearest-neighbor search to compute the symmetric distortion:

$$\begin{cases} D_{\text{classic}}(\mathbf{P}^O, \mathbf{P}^D) = \max\{d_{O \rightarrow D}, d_{D \rightarrow O}\} \\ d_{O \rightarrow D} = \frac{1}{N_O} \sum_{i=1}^{N_O} \left\| M_O(\mathbf{p}_i^O) - M_D(\varphi_{O \rightarrow D}(\mathbf{p}_i^O)) \right\|_2, \\ d_{D \rightarrow O} = \frac{1}{N_D} \sum_{j=1}^{N_D} \left\| M_D(\mathbf{p}_j^D) - M_O(\varphi_{D \rightarrow O}(\mathbf{p}_j^D)) \right\|_2 \end{cases} \quad (3)$$

where $\varphi_{O \rightarrow D}$ denotes the injective mapping determined by nearest-neighbor search. Due to the unordered nature of point cloud data and the random distribution of points in space, a simple nearest-neighbor search may result in incorrect mapping. For example, if the points in \mathbf{P}^O are denser than those in \mathbf{P}^D or if there is a spatial distribution bias between the two, the

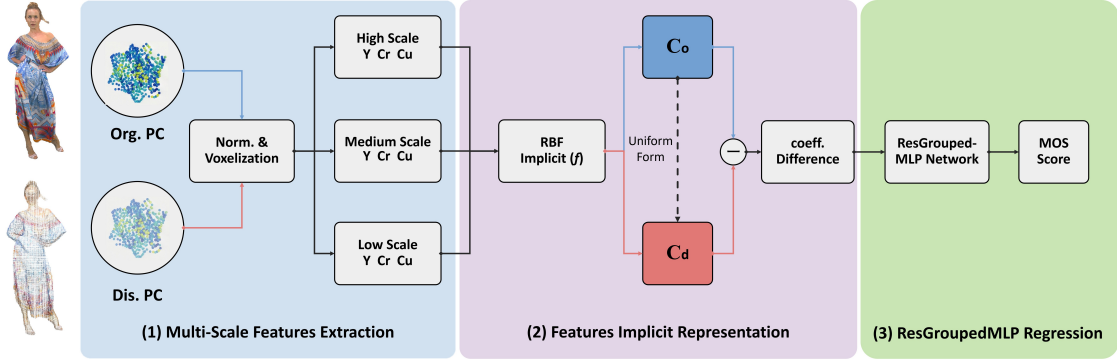


Fig. 2. The schematic diagram depicts implementing the MS-ISSM solution. (1) Multi-scale features are extracted from the normalized distorted and original point clouds. The chroma, luma, and curvature features of each point cloud are calculated under high-, medium-, and low-quality conditions. (2) The RBF implicit representation is used to calculate the coefficient values for each feature, and multi-scale feature coefficient differences are calculated. (3) The ResGrouped-MLP is designed to map the multi-scale features coefficient differences to perceptual quality scores.

nearest-neighbor search leads to inaccurate matches. This, in turn, would affect the calculation of feature differences and, ultimately, the distortion measurement. To achieve accurate feature correspondence, in our earlier work [17], we obtained a bijective set of point features by using a feature interpolation function. However, this method only utilized single-scale luminance values. Additionally, the point-based methods struggle to account for changes in the local structure of the point cloud, leading to distortion results that differ from actual perception.

B. Feature Implicit Representation and Multi-scale Perceptual Distortion Calculation

To address the above challenges, considering that exact point-to-point correspondence is difficult to achieve, for a local space, we map the feature set of the point cloud to a feature function, as shown in:

$$\begin{cases} \{\mathbf{p}_i^O, M_O(\mathbf{p}_i^O)\}_{i=1}^{N_O} \rightarrow f^O(\mathbf{p}_i^O, \mathbf{W}^O) = M_O(\mathbf{p}_i^O) \\ \{\mathbf{p}_j^D, M_D(\mathbf{p}_j^D)\}_{j=1}^{N_D} \rightarrow f^D(\mathbf{p}_j^D, \mathbf{W}^D) = M_D(\mathbf{p}_j^D) \end{cases}, \quad (4)$$

where $f^O(\mathbf{p}_i^O, \mathbf{W}^O)$ and $f^D(\mathbf{p}_j^D, \mathbf{W}^D)$ represent the feature functions of the original and distorted point clouds, respectively. $\mathbf{W}^O = \{w_k^O\}_{k=1}^K$ and $\mathbf{W}^D = \{w_k^D\}_{k=1}^K$ are the coefficient matrices of the implicit functions of \mathbf{P}^O and \mathbf{P}^D , respectively. This approach transforms the feature difference into the error between their corresponding feature functions.

Since $\mathbf{W}^O = \{w_k^O\}_{k=1}^K$ and $\mathbf{W}^D = \{w_k^D\}_{k=1}^K$ have the same functional form, we calculate the feature function difference by the implicit function coefficients, as shown in:

$$\begin{cases} D'(\mathbf{P}^O, \mathbf{P}^D) = g(d_1, \dots, d_k, \dots, d_K) \\ d_k = \left| \frac{w_k^O - w_k^D}{\max\{|w_k^O|, |w_k^D|\} + \tau} \right| \end{cases}, \quad (5)$$

where $\tau = 10^{-5}$ prevents division by zero, and d_k represents the difference between the individual function coefficients, and $g()$ is the nonlinear mapping from the feature function coefficient differences to the perceptual difference, and this mapping is obtained through a regression model. This method addresses the difficulty of point-to-point correspondence matching while considering the structural changes in local features.

Furthermore, considering the multi-scale nature of human visual perception, we incorporate the differences at low, medium, and high scales into the final distortion calculation. The final distortion is expressed as:

$$D_{pro} = g \left(\underbrace{d_1, \dots, d_K}_L, \underbrace{d_1, \dots, d_K}_M, \underbrace{d_1, \dots, d_K}_H \right). \quad (6)$$

IV. PROPOSED MS-ISSM

In this section, we first present the general framework of the proposed MS-ISSM in subsection A. Then, the implementation details of each module are described in subsections B – D, respectively.

A. Overview

Due to the complexity of the human visual system (HVS), extracting features from point clouds and mapping them to precise perceptual quality metrics is a challenging task [22]. To address this issue and streamline the computation process, we approach it in three steps.

In the first step, we extract multi-scale features from the normalized distorted and original point clouds. We focus on the chroma, luma, and curvature features of each point cloud under high-, medium-, and low-quality conditions.

In the second step, we apply the RBF implicit representation to the spatial scale features of the obtained distorted point cloud and the original point cloud, calculating the coefficient values for each feature's implicit representation.

In the third step, we propose the ResGrouped-MLP to map the multi-scale feature coefficient differences to perceptual quality scores.

The overall process of the proposed MS-ISSM is illustrated in Fig. 2.

B. Multi-scale Features Extraction

To capture complex perceptual changes, we utilize three physical features that align with the HVS: curvature, luma, and chroma. Curvature describes the local surface geometry,

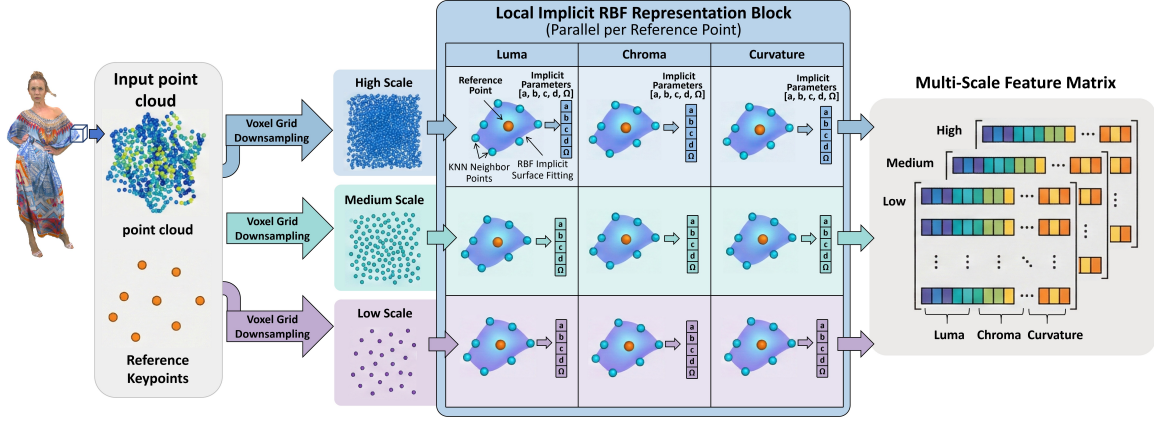


Fig. 3. Schematic illustration of the Multi-scale implicit feature extraction framework for point cloud.

reflecting sensitivity to both fine details and global structure [21]. Luma and chroma, calculated from the point cloud’s color components [7], represent light intensity and color distribution, respectively.

To ensure generalization across varying geometric scales, we normalize the geometric components of both distorted and original point clouds as follows:

$$\hat{\mathbf{p}}_n^\alpha = \frac{1024 \cdot (\mathbf{p}_n^\alpha - \mathbf{p}_{\min})}{L_{\max}}, \quad (7)$$

where $\hat{\mathbf{p}}_n^\alpha$ denotes the normalized coordinates. L_{\max} is the maximum edge length of the bounding box of the original point cloud \mathbf{P}^O , and \mathbf{p}_{\min} is the coordinate-wise minimum vector. The resulting normalized point cloud is denoted as $\hat{\mathbf{P}}^\alpha = \{\hat{\mathbf{p}}_n^\alpha, \mathbf{q}_n^\alpha\}$.

Furthermore, inspired by the multi-layered perceptual mechanism of human vision, multi-scale point clouds are generated from both the original and distorted inputs through voxel grid downsampling. The voxel sizes are set to 2.0, 4.0, and 8.0, respectively. The base voxel size of 2.0 is selected as the trade-off between capturing high-frequency structural details and maintaining computational efficiency. These values follow a dyadic progression, consistent with the hierarchical octree decomposition widely used in point cloud compression standards [7]. This geometric progression allows for a systematic separation of spatial frequency components: the smallest scale captures high-frequency details (e.g., texture and noise), while the largest scale retains low-frequency structural information (e.g., global shape), ensuring a comprehensive evaluation of perceptual quality. Mimicking the way human vision adapts to different environments, this method focuses on various levels of detail, as shown in Fig. 3.

C. Feature Implicit Representation

The features of the local point cloud are implicitly represented using RBF [42]:

$$f_{\mathbf{F}}^{\alpha,\beta}(\hat{\mathbf{p}}^{\alpha,\beta}) = \eta_{\mathbf{F}}^{\alpha,\beta}(\hat{\mathbf{p}}^{\alpha,\beta}) + \sum_{n=1}^{N_{\beta}^{\alpha}} \left[\omega_{\mathbf{F},n}^{\alpha,\beta} \cdot \phi^{\alpha,\beta}(\|\hat{\mathbf{p}}^{\alpha,\beta} - \hat{\mathbf{p}}_n^{\alpha,\beta}\|_2) \right], \quad (8)$$

where $\beta \in \{H, M, L\}$ represents the type of different spatial scales: high, medium, and low. $\mathbf{F} \in \{Cu, Y, Cr\}$ denotes feature types: curvature, luma, and chroma, and $N^{\alpha,\beta}$ indicates the number of points that influence the implicit function. $f_{\mathbf{F}}^{\alpha,\beta}(\hat{\mathbf{p}}^{\alpha,\beta})$ corresponds to the implicit function associated with the current feature $\mathbf{F}^{\alpha,\beta}$, and $\hat{\mathbf{p}}^{\alpha,\beta} \in \hat{\mathbf{P}}^{\alpha,\beta}$. $\omega_{\mathbf{F},n}^{\alpha,\beta}$ denote the weight coefficients. $\phi^{\alpha,\beta}(\cdot)$ denotes the RBF kernel function, defined as

$$\phi^{\alpha,\beta}(\|\hat{\mathbf{p}}^{\alpha,\beta} - \hat{\mathbf{p}}_n^{\alpha,\beta}\|_2) = \exp\left(-0.5\|\hat{\mathbf{p}}^{\alpha,\beta} - \hat{\mathbf{p}}_n^{\alpha,\beta}\|_2^2\right). \quad (9)$$

The Gaussian kernel function is chosen by its effectiveness and stability for localized point cloud feature representation [17]. And $\eta_{\mathbf{F}}^{\alpha,\beta}(\hat{\mathbf{p}}^{\alpha,\beta})$ is a three-variable polynomial with a maximum degree of 3. It is commonly expressed as

$$\eta_{\mathbf{F}}^{\alpha,\beta}(\hat{\mathbf{p}}^{\alpha,\beta}) = a_{\mathbf{F}}^{\alpha,\beta} \cdot \hat{x}^{\alpha,\beta} + b_{\mathbf{F}}^{\alpha,\beta} \cdot \hat{y}^{\alpha,\beta} + c_{\mathbf{F}}^{\alpha,\beta} \cdot \hat{z}^{\alpha,\beta} + d_{\mathbf{F}}^{\alpha,\beta}, \quad (10)$$

where $a_{\mathbf{F}}^{\alpha,\beta}, b_{\mathbf{F}}^{\alpha,\beta}, c_{\mathbf{F}}^{\alpha,\beta}, d_{\mathbf{F}}^{\alpha,\beta}$ are constant coefficients. $\hat{x}^{\alpha,\beta}, \hat{y}^{\alpha,\beta}$, and $\hat{z}^{\alpha,\beta}$ represent coordinates of point $\hat{\mathbf{p}}^{\alpha,\beta}$ at x, y, z directions, respectively.

To ensure a non-singular coefficient matrix for a unique solution and prevent the RBF kernel from interfering with the polynomial terms, the weight coefficients $\omega_{\mathbf{F},n}^{\alpha,\beta}$ must satisfy the following constraint conditions:

$$\sum_{n=1}^{N^{\alpha,\beta}} \omega_{\mathbf{F},n}^{\alpha,\beta} = \sum_{n=1}^{N^{\alpha,\beta}} \omega_{\mathbf{F},n}^{\alpha,\beta} \hat{x}_n^{\alpha,\beta} = \sum_{n=1}^{N^{\alpha,\beta}} \omega_{\mathbf{F},n}^{\alpha,\beta} \hat{y}_n^{\alpha,\beta} = \sum_{n=1}^{N^{\alpha,\beta}} \omega_{\mathbf{F},n}^{\alpha,\beta} \hat{z}_n^{\alpha,\beta} = 0. \quad (11)$$

And by inputting all coordinates of $\hat{\mathbf{p}}^{\alpha,\beta}$ in $\hat{\mathbf{P}}^{\alpha,\beta}$ into Eq. (8), we determine the coefficients of $\eta_{\mathbf{F}}^{\alpha,\beta}(\hat{\mathbf{p}}^{\alpha,\beta})$ and $\omega_{\mathbf{F},n}^{\alpha,\beta}$ through the following equation:

$$\mathbf{X}^{\alpha,\beta} \cdot \mathbf{W}_{\mathbf{F}}^{\alpha,\beta} = \mathbf{Y}_{\mathbf{F}}^{\alpha,\beta}. \quad (12)$$

In our implementation, we use Householder QR decomposition to solve Eq. (12), preventing the numerical instability of direct matrix inversion. $\mathbf{Y}_{\mathbf{F}}^{\alpha,\beta}$ is the feature matrix, as shown in

$$\mathbf{Y}_{\mathbf{F}}^{\alpha,\beta} = \begin{bmatrix} \mathbf{F}^{\alpha,\beta}(\hat{\mathbf{p}}_1^{\alpha,\beta}) & \dots & \mathbf{F}^{\alpha,\beta}(\hat{\mathbf{p}}_{N^{\alpha,\beta}}^{\alpha,\beta}) & \mathbf{0} \end{bmatrix}^\top. \quad (13)$$

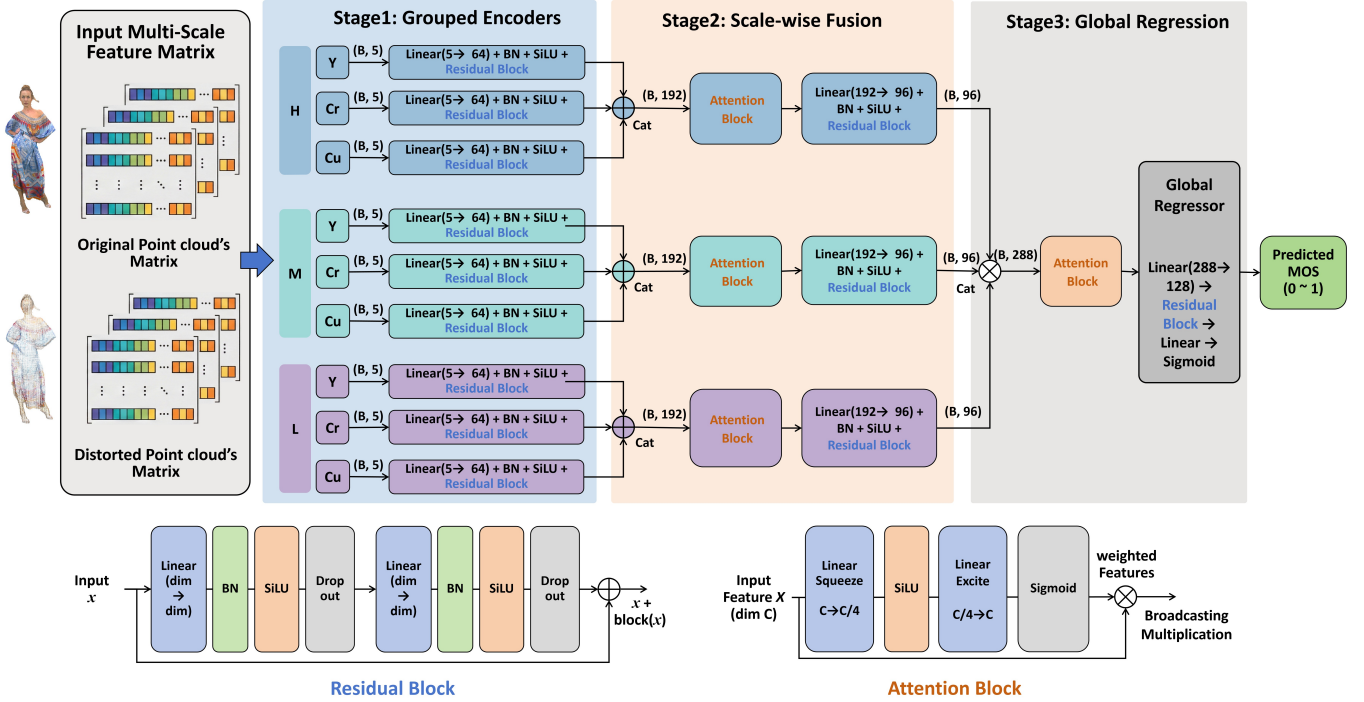


Fig. 4. The Proposed ResGrouped-MLP Network.

$\mathbf{X}^{\alpha,\beta}$ is the coordinate matrix, as represented in

$$\mathbf{X}^{\alpha,\beta} = \begin{bmatrix} \phi_{11}^{\alpha,\beta} & \cdots & \phi_{1N^{\alpha,\beta}}^{\alpha,\beta} & \hat{x}_1^{\alpha,\beta} & \hat{y}_1^{\alpha,\beta} & \hat{z}_1^{\alpha,\beta} & 1 \\ \vdots & \ddots & \vdots & \vdots & \vdots & \vdots & \vdots \\ \phi_{N^{\alpha,\beta}1}^{\alpha,\beta} & \cdots & \phi_{N^{\alpha,\beta}N^{\alpha,\beta}}^{\alpha,\beta} & \hat{x}_{N^{\alpha,\beta}}^{\alpha,\beta} & \hat{y}_{N^{\alpha,\beta}}^{\alpha,\beta} & \hat{z}_{N^{\alpha,\beta}}^{\alpha,\beta} & 1 \\ 1 & \cdots & 1 & 0 & 0 & 0 & 0 \\ \hat{x}_1^{\alpha,\beta} & \cdots & \hat{x}_{N^{\alpha,\beta}}^{\alpha,\beta} & 0 & 0 & 0 & 0 \\ \hat{y}_1^{\alpha,\beta} & \cdots & \hat{y}_{N^{\alpha,\beta}}^{\alpha,\beta} & 0 & 0 & 0 & 0 \\ \hat{z}_1^{\alpha,\beta} & \cdots & \hat{z}_{N^{\alpha,\beta}}^{\alpha,\beta} & 0 & 0 & 0 & 0 \end{bmatrix} \quad (14)$$

where $\phi_{12}^{\alpha,\beta}$ is equal to $\phi^{\alpha,\beta} \left(\left\| \hat{\mathbf{p}}_1^{\alpha,\beta} - \hat{\mathbf{p}}_2^{\alpha,\beta} \right\|_2 \right)$. And $\mathbf{W}_F^{\alpha,\beta}$ is the weight matrix, as represented in

$$\mathbf{W}_F^{\alpha,\beta} = \left[\omega_{F,1}^{\alpha,\beta} \cdots \omega_{F,N^{\alpha,\beta}}^{\alpha,\beta} a_F^{\alpha,\beta} b_F^{\alpha,\beta} c_F^{\alpha,\beta} d_F^{\alpha,\beta} \right]^T. \quad (15)$$

Since the number of coefficients in the weight matrix $\mathbf{W}_F^{\alpha,\beta}$ is determined by the number of points $N^{\alpha,\beta}$, to simplify the computational process and facilitate the comparison of distortions using the coefficients, we downsample $\hat{\mathbf{P}}^O$ to obtain a set of reference points, denoted as $\mathbf{P}^R = \{\mathbf{p}_t^R\}_{t=1}^{N_R}$. Using nearest-neighbor search, for each point \mathbf{p}_t^R in the reference point set, we find the 30 closest neighbors in both $\{\hat{\mathbf{p}}_i^O\}_{i=1}^{N_O}$ and $\{\hat{\mathbf{p}}_j^D\}_{j=1}^{N_D}$, which are then used to compute the implicit function for the region around each reference point. Finally, the features of $\hat{\mathbf{P}}^O$ and $\hat{\mathbf{P}}^D$ can be represented as tensors \mathbf{C}^α :

$$\mathbf{C}^\alpha = \begin{bmatrix} \mathbf{W}_{C_u}^{\alpha,H} & \mathbf{W}_Y^{\alpha,H} & \mathbf{W}_{C_r}^{\alpha,H} \\ \mathbf{W}_{C_u}^{\alpha,M} & \mathbf{W}_Y^{\alpha,M} & \mathbf{W}_{C_r}^{\alpha,M} \\ \mathbf{W}_{C_u}^{\alpha,L} & \mathbf{W}_Y^{\alpha,L} & \mathbf{W}_{C_r}^{\alpha,L} \end{bmatrix}. \quad (16)$$

By substituting \mathbf{C}^O and \mathbf{C}^D into Eq. (5) and (6), the quality score of \mathbf{P}^D is calculated. Considering the simplicity of the

algorithm and to avoid an excessive number of comparison coefficients, we take the average of weight coefficients differences. And the function $g()$ is obtained through the ResGrouped-MLP network as follow.

D. ResGrouped-MLP Regression

We propose the ResGrouped-MLP, a hierarchical deep learning framework designed to robustly map hand-crafted point cloud features to subjective quality scores. Addressing the limitations of flat networks, we adopt a "Split-Transform-Merge" architecture to preserve the distinct physical semantics of features. The framework integrates a novel Log-Modulus preprocessing and a multi-scale attention mechanism, as shown in Fig. 4.

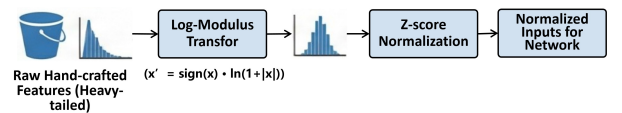


Fig. 5. Preprocessing pipeline of hand-crafted features

Log-Modulus Preprocessing: Statistical features extracted from point clouds often exhibit a heavy-tailed distribution, where standard Z-score normalization can lead to gradient instability and poor convergence. To address this, we selected the Log-Modulus transformation to handle signed data and compress heavy-tailed distributions caused by local distortions. This parameter-free operation improves network training stability as follows:

$$x' = \text{sign}(x) \cdot \ln(1 + |x|), \quad (17)$$

where x denotes the raw feature value. This transformation effectively rectifies the data distribution towards a quasi-normal form, allowing the subsequent network to focus on underlying feature patterns rather than being biased by outliers, as shown in Fig. 5.

The ResGrouped-MLP Architecture: Point cloud quality perception relies on the interplay between feature scales (High, Medium, Low) and attribute channels (luma, chroma, curvatures). Simply concatenating these features risks losing their distinct physical meanings. Therefore, we design a hierarchical architecture composed of three key stages:

a) Deep Grouped Encoders: Instead of a generic fully connected layer, we treat each scale-channel pair as an independent group. We employ Residual Blocks for feature encoding, formulated as $x + \mathcal{F}(x)$, where $\mathcal{F}(\cdot)$ represents a dual-layer perceptron with Batch Normalization and SiLU activation. This grouped design isolates the specific distortion characteristics of each channel, preventing information interference at early stages while mitigating the vanishing gradient problem.

b) Scale-wise Attention Fusion: Since different color channels contribute unequally to human perception, we introduce a Channel Attention Block to recalibrate features within each scale. The mechanism adaptively learns weights to highlight salient distortions:

$$\mathbf{f}_{scale}' = \mathbf{f}_{scale} \otimes \sigma(\text{MLP}(\mathbf{f}_{scale})), \quad (18)$$

where \mathbf{f}_{scale} is the concatenated feature vector, \otimes denotes element-wise multiplication, and $\sigma(\cdot)$ is the Sigmoid function. The internal MLP utilizes a bottleneck structure with a reduction ratio $r = 4$. This bottleneck compresses the feature space to aggregate global information before restoring it, enabling the network to dynamically suppress noise and emphasize the most relevant feature channels.

c) Global Hierarchical Regression: Finally, the refined features from H, M, and L scales are concatenated and passed through a Global Attention module. This ensures the model captures the complex interaction between global geometry (Low scale) and local fine-grained details (High scale) before mapping them to the final quality score.

Loss Function: To ensure prediction accuracy, linearity, and monotonic consistency, we utilize a hybrid loss function combining mean squared error (MSE), Pearson Linear Correlation Coefficient (PLCC) loss, and Margin Ranking loss:

$$\mathcal{L}_{total} = \mathcal{L}_{MSE} + \lambda_1 \mathcal{L}_{PLCC} + \lambda_2 \mathcal{L}_{Rank}, \quad (19)$$

where λ_1 and λ_2 are weighting parameters used to balance the optimization objectives. And, these values are set to 0.2 and 0.2, respectively. Such a configuration ensures that the PLCC loss provides strong linear correlation guidance and the Margin Ranking loss penalizes monotonicity violations without overwhelming the primary MSE regression.

Implementation and Validation: The model is trained using the AdamW optimizer with a weight decay of 10^{-2} and a Cosine Annealing scheduler for 80 epochs (batch size 32). The detailed hyperparameter configurations, including the grouped encoders, scale-wise attention and global regressor, are summarized in Table I.

TABLE I
DETAILED CONFIGURATIONS OF THE RESGROUPED-MLP.

Module	Sequential Operations
grouped encoders	FC (64), BN, SiLU, ResBlock (dropout = 0.1)
scale-wise attention	FC (48), SiLU, FC (192), sigmoid
global regressor	FC (128), BN, SiLU, ResBlock (dropout = 0.2), FC (64), SiLU, FC (1), sigmoid

V. EXPERIMENTAL EVALUATIONS

This section uses four publicly available point cloud subjective datasets to validate the proposed method’s effectiveness in perceptual evaluation. We compare the quality assessment results of our method with those of classic and state-of-the-art (SOTA) PCQA metrics. By analyzing the results across various datasets, we can assess the robustness and generalization of our method in different distortions.

A. Evaluation Criteria

To ensure alignment between the subjective ratings and objective predictions of different metrics, we standardize the objective predictions to a consistent dynamic range based on guidance from the video quality expert group (VQEG) [43]. Subsequently, we use Pearson’s linear correlation coefficient (PLCC), Spearman’s rank order correlation coefficient (SROCC), Kendall’s rank order correlation coefficient (KROCC), and root mean square error (RMSE) to evaluate the performance of various metrics, representing their linearity, monotonicity, and accuracy, respectively. Higher PLCC, SROCC, and KROCC values indicate superior metric performance, while lower RMSE values suggest better accuracy. To normalize the scores of objective quality assessment metrics onto a uniform scale, we apply the logistic regression method recommended by VQEG.

B. Datasets and PCQA Metrics

To verify the performance of the proposed method across different types of distortions, we use four point cloud subjective datasets for assessment. These datasets include: SJTU [10], WPC [40], M-PCCD [44], and ICIP [45]. Moreover, to optimize the regression model and guarantee strict content separation, we employed a K-fold cross-validation strategy on each dataset [37]. To accommodate the varying sizes of the datasets, the number of folds was explicitly tailored: we utilized 6-fold cross-validation for the ICIP dataset, 8-fold for M-PCCD, 9-fold for SJTU, and 10-fold for WPC. Performance is evaluated using two distinct aggregation methods. The first, denoted as “K-fold average”, computes the PLCC, SROCC, KROCC, and RMSE metrics per fold and averages them. The second, denoted as “K-fold splicing”, concatenates the out-of-sample prediction scores for all point clouds across the K-fold iterations to compute the evaluation metrics globally at once [37]. In addition, this paper compares the proposed algorithm with 12 classic and SOTA PCQA metrics. It is worth

TABLE II

PERFORMANCE COMPARISON OF DIFFERENT PCQA METRICS. THE BEST, SECOND-BEST, AND THIRD-BEST AMONG THE PRIMARY METHODS ARE HIGHLIGHTED IN RED, BLUE, AND UNDERLINED, RESPECTIVELY.

Method	Crit.	Datasets				Rank
		SJTU [10]	ICIP [45]	M-PCCD [44]	WPC [40]	
PSNR-p2p [7]	PLCC	0.460	0.862	0.395	0.260	12.25
	SROCC	0.398	0.853	0.239	0.008	12.00
	KROCC	0.298	0.590	0.196	0.002	12.75
	RMSE	2.130	0.659	1.250	22.137	12.50
PSNR-p2pl [7]	PLCC	0.433	0.898	0.395	0.260	11.75
	SROCC	0.415	0.843	0.232	0.053	12.00
	KROCC	0.303	0.606	0.201	0.034	11.75
	RMSE	2.162	0.642	1.250	22.137	11.75
PSNR-YUV [7]	PLCC	0.550	0.779	0.603	0.387	11.50
	SROCC	0.555	0.777	0.620	0.384	11.50
	KROCC	0.385	0.580	0.442	0.263	11.50
	RMSE	2.003	0.712	1.085	21.139	11.50
PSSIM [27]	PLCC	0.769	0.886	0.712	0.500	10.00
	SROCC	0.717	0.877	0.716	0.424	9.75
	KROCC	0.522	0.701	0.538	0.300	9.75
	RMSE	1.533	0.653	0.956	19.854	10.25
PCQM [14]	PLCC	0.807	0.948	0.903	0.563	6.75
	SROCC	0.774	0.956	0.916	0.545	6.50
	KROCC	0.590	0.830	0.748	0.432	7.25
	RMSE	1.418	0.363	0.584	18.947	7.00
MS-PSSIM [31]	PLCC	0.844	0.929	0.768	0.551	7.50
	SROCC	0.842	0.906	0.777	0.541	7.50
	KROCC	0.645	0.771	0.602	0.381	7.25
	RMSE	1.286	0.612	0.872	19.132	8.25
GraphSIM [25]	PLCC	0.860	0.901	0.921	0.690	6.00
	SROCC	0.843	0.888	0.936	0.679	6.25
	KROCC	0.641	0.723	0.786	0.493	6.50
	RMSE	1.223	0.492	0.529	16.597	6.00
MS-GraphSIM [26]	PLCC	0.897	0.902	0.906	0.702	5.75
	SROCC	0.874	0.890	0.922	0.701	5.75
	KROCC	0.682	0.727	0.761	0.517	6.00
	RMSE	1.058	0.491	0.575	16.324	5.50
PHM [30]	PLCC	0.901	0.867	0.945	0.838	4.50
	SROCC	0.880	0.831	0.948	0.832	4.75
	KROCC	0.695	0.701	0.807	0.639	4.50
	RMSE	1.038	0.566	0.445	12.509	4.00
TCDM [29]	PLCC	0.931	0.942	0.937	0.805	3.50
	SROCC	0.912	0.935	0.945	0.803	3.75
	KROCC	0.740	0.803	0.801	0.604	3.75
	RMSE	0.875	0.381	0.475	13.607	4.00
FRSVR (K-fold splicing) [36]	PLCC	0.822	0.957	0.886	0.825	5.00
	SROCC	0.806	0.954	0.904	0.827	5.25
	KROCC	0.601	0.843	0.783	0.620	4.50
	RMSE	1.333	0.341	0.341	12.786	3.25
PointPCA (K-fold splicing) [34]	PLCC	0.819	0.942	0.912	0.806	5.25
	SROCC	0.786	0.946	0.946	0.807	4.75
	KROCC	0.592	0.837	0.827	0.607	4.25
	RMSE	1.341	0.375	0.375	13.456	4.75
MS-ISSM (K-fold splicing)	PLCC	0.906	0.964	0.958	0.855	1.25
	SROCC	0.897	0.967	0.961	0.846	1.25
	KROCC	0.698	0.852	0.853	0.666	1.25
	RMSE	1.224	0.283	0.351	11.736	2.25
FRSVR (K-fold average) [36]	PLCC	0.858	0.976	0.916	0.842	-
	SROCC	0.823	0.969	0.929	0.836	-
	KROCC	0.622	0.893	0.778	0.647	-
	RMSE	1.279	0.279	0.432	12.143	-
PointPCA (K-fold average) [34]	PLCC	0.847	0.976	0.956	0.812	-
	SROCC	0.842	0.974	0.964	0.815	-
	KROCC	0.625	0.855	0.855	0.614	-
	RMSE	1.293	0.269	0.339	13.078	-
MS-ISSM (K-fold average)	PLCC	0.925	0.968	0.966	0.867	-
	SROCC	0.911	0.976	0.971	0.859	-
	KROCC	0.763	0.917	0.883	0.661	-
	RMSE	1.043	0.256	0.344	11.618	-

TABLE III

PERFORMANCE COMPARISON OF CLASSIC AND SOTA METRICS ON DIFFERENT DISTORTION TYPES. THE BEST, SECOND-BEST, AND THIRD-BEST ARE HIGHLIGHTED IN RED, BLUE, AND UNDERLINED, RESPECTIVELY.

Method	Crit.	Distortion types					
		Ds	Ns	Oc	Mx	Tc	Vc
PSNR-p2p	PLCC	0.394	0.649	0.525	0.737	0.468	0.208
	SROCC	0.333	0.649	0.368	0.673	0.440	0.196
	KROCC	0.232	0.482	0.267	0.513	0.311	0.133
	RMSE	1.330	0.806	1.082	0.851	1.115	0.893
PSNR-p2pl	PLCC	0.296	0.672	0.527	0.666	0.471	0.264
	SROCC	0.188	0.668	0.373	0.636	0.437	0.243
	KROCC	0.135	0.494	0.270	0.473	0.310	0.166
	RMSE	1.383	0.784	1.080	0.939	1.114	0.881
PSNR-YUV	PLCC	0.632	0.588	0.561	0.670	0.541	0.393
	SROCC	0.617	0.559	0.543	0.659	0.528	0.391
	KROCC	0.421	0.404	0.364	0.490	0.369	0.267
	RMSE	1.122	0.856	1.052	0.934	1.062	0.840
PSSIM	PLCC	0.959	0.771	0.728	0.881	0.464	0.303
	SROCC	0.906	0.766	0.564	0.877	0.091	0.166
	KROCC	0.719	0.585	0.431	0.691	0.062	0.112
	RMSE	0.413	0.675	0.872	0.595	1.118	0.870
PCQM	PLCC	0.435	0.900	0.870	0.902	0.718	0.643
	SROCC	0.054	0.902	0.872	0.881	0.714	0.623
	KROCC	0.047	0.720	0.683	0.691	0.519	0.443
	RMSE	1.303	0.462	0.627	0.544	0.879	0.700
MS-PSSIM	PLCC	0.703	0.758	0.753	0.880	0.611	0.359
	SROCC	0.689	0.737	0.745	0.865	0.565	0.338
	KROCC	0.516	0.539	0.551	0.675	0.399	0.233
	RMSE	1.029	0.690	0.836	0.597	0.999	0.852
GraphSIM	PLCC	0.943	0.885	0.854	0.895	0.628	0.637
	SROCC	0.891	0.883	0.844	0.872	0.631	0.619
	KROCC	0.685	0.691	0.663	0.670	0.462	0.442
	RMSE	0.480	0.492	0.662	0.562	0.983	0.704
MS-GraphSIM	PLCC	0.945	0.892	0.877	0.918	0.616	0.673
	SROCC	0.893	0.890	0.865	0.898	0.623	0.662
	KROCC	0.693	0.701	0.680	0.709	0.459	0.479
	RMSE	0.472	0.478	0.610	0.499	0.995	0.675
PHM	PLCC	0.950	0.916	0.901	0.941	0.772	0.696
	SROCC	0.905	0.909	0.895	0.932	0.769	0.676
	KROCC	0.714	0.735	0.716	0.774	0.575	0.488
	RMSE	0.452	0.425	0.552	0.425	0.803	0.656
TCDM	PLCC	0.943	0.904	0.899	0.952	0.821	0.689
	SROCC	0.891	0.903	0.883	0.939	0.818	0.678
	KROCC	0.697	0.722	0.710	0.782	0.622	0.493
	RMSE	0.481	0.454	0.558	0.385	0.721	0.661
FRSVR (K-fold splicing)	PLCC	0.952	0.850	0.911	0.833	0.890	0.733
	SROCC	0.902	0.864	0.906	0.829	0.879	0.730
	KROCC	0.716	0.678	0.733	0.638	0.654	0.522
	RMSE	0.466	0.523	0.511	0.635	0.652	0.621
PointPCA (K-fold splicing)	PLCC	0.942	0.847	0.879	0.820	0.842	0.655
	SROCC	0.891	0.859	0.885	0.819	0.823	0.671
	KROCC	0.703	0.679	0.702	0.634	0.611	0.481
	RMSE	0.471	0.517	0.572	0.627	0.711	0.669
MS-ISSM (K-fold splicing)	PLCC	0.954	0.876	0.933	0.916	0.902	0.783
	SROCC	0.890	0.862	0.923	0.889	0.904	0.754
	KROCC	0.695	0.689	0.767	0.699	0.730	0.562
	RMSE	0.432	0.512	0.459	0.529	0.545	0.568

noting that PointPCA [34] and FRVSR [36] are learning-based methods, and their training and testing follow the same procedures as the proposed method.

C. Performance Comparison

We evaluate the performance of various PCQA metrics using different datasets. The overall evaluation results for each PCQA metric across these datasets are presented in Table II. To facilitate direct comparison, the best, second-best, and third-best performing metrics are highlighted in

red, blue, and underlined text, respectively. Notably, the K-fold average results of the learning-based methods are excluded from the comparison and ranking. Instead, the rankings rely on the global concatenated results using splicing. This approach aggregates predictions from all test folds before calculating the final correlation. It ensures a fair comparison with traditional hand-crafted metrics evaluated on the entire dataset. Specifically, the proposed method ranks highest on the WPC dataset compared to the other PCQA metrics. On the M-PCCD dataset, the proposed method achieves first place in PLCC, SROCC, and KROCC. On the ICIP dataset, it achieves the best performance in PLCC, SROCC, KROCC, and RMSE. Although the proposed method does not achieve the best performance on the SJTU dataset, it closely trails the top-performing TCDM method. On the SJTU dataset, MS-ISSM yields a PLCC of 0.906 and an SROCC of 0.897, compared with the best-performing method, TCDM, which achieves 0.931 and 0.912. Notably, based on the overall rank across all four datasets, the proposed method demonstrates the best performance. It is followed by TCDM, which achieve competitive but lower correlations. Furthermore, compared with other learning-based methods, our method demonstrates better overall performance in both K-fold average and K-fold splicing results. Overall, the proposed method is demonstrated with advanced performance.

We combine four datasets to validate metric performance across distortion types. Because subjective rating scales differ, we map all scores onto a common scale of 0 to 5 for consistency. Table III presents the results across distortions including octree-based compression (Oc), video-based compression (Vc), trisoup-based compression (Tc), noise (Ns), downsampling (Ds), and mixing (Mix). As with previous tables, the best, second-best, and third-best performing metrics highlighted in red, blue, and underlined text. Overall, the proposed MS-ISSM exhibits strong performance in octree-based compression, trisoup-based compression, and video-based compression. Specifically, it achieves the highest PLCC, SROCC, KROCC, and RMSE in these three categories. For downsampling distortion, MS-ISSM performs competitively, securing the second-best PLCC and RMSE.

Regarding mixing distortion, MS-ISSM performs lower than TCDM. The mixing distortion samples originate entirely from the SJTU dataset, where TCDM parameters were explicitly fitted, providing a distributional advantage. However, in the video-based compression scenario, MS-ISSM maintains a clear lead. While FRSVR obtains an SROCC of 0.730 and an RMSE of 0.621, MS-ISSM reaches a higher SROCC of 0.754 and a lower RMSE of 0.568.

In overall, MS-ISSM achieves the strong performance across different distortion types. This generalization capability confirms the effectiveness of our design in three key aspects. First, the RBF-based implicit representation reconstructs continuous surfaces to resolve sparsity and geometric jitter. This bypasses discrete point-to-point matching errors, yielding superior stability in V-PCC and compression distortions. Second, our hierarchical approach captures both global structural shifts from downsampling and local high-frequency artifacts from compression. Finally, the ResGrouped-MLP combines

Log-Modulus transformation for distribution rectification with channel-wise attention for adaptive feature weighting, ensuring robust prediction in mixed distortion scenarios.

Additionally, to further compare the performance of the MS-ISSM method and the RBFIM method in terms of compression distortion, we evaluated datasets containing compression distortion from the three aforementioned datasets. Based on the type of compression distortion, the datasets were divided into G-PCC compression distortion and V-PCC compression distortion. Table IV shows that RBFIM performs better on both subsets of the ICIP dataset. However, MS-ISSM outperforms RBFIM on the G-PCC and V-PCC subsets of the WPC and M-PCCD datasets. Furthermore, MS-ISSM achieves higher correlations and lower errors on the combined ALL dataset. This indicates that the multi-scale implicit feature method provides stable generalization across diverse compression scenarios.

TABLE IV
COMPARISON OF THE RBFIM AND MS-ISSM (K-FOLD SPLICING)
METHODS UNDER DIFFERENT COMPRESSION DISTORTIONS.

Datasets	criteria	RBFIM [17]	MS-ISSM
ICIP-GPCC	PLCC	0.993	0.975
	SROCC	0.971	0.968
	KROCC	0.870	0.846
	RMSE	0.020	0.027
ICIP-VPCC	PLCC	0.969	0.969
	SROCC	0.976	0.956
	KROCC	0.895	0.840
WPC-GPCC	RMSE	0.067	0.130
	PLCC	0.841	0.865
	SROCC	0.847	0.864
WPC-VPCC	KROCC	0.655	0.677
	RMSE	0.193	0.165
	PLCC	0.482	0.683
MPCCD-GPCC	SROCC	0.473	0.638
	KROCC	0.343	0.461
	RMSE	0.190	0.176
MPCCD-VPCC	PLCC	0.734	0.977
	SROCC	0.673	0.974
	KROCC	0.544	0.866
ALL	RMSE	0.280	0.096
	PLCC	0.489	0.921
	SROCC	0.460	0.904
ALL	KROCC	0.288	0.750
	RMSE	0.245	0.117
	PLCC	0.611	0.892
ALL	SROCC	0.566	0.892
	KROCC	0.406	0.718
	RMSE	0.259	0.159

D. Visual Comparisons

To illustrate the perceptual performance of MS-ISSM against existing methods, we present a qualitative comparison in Fig. 6. We selected four representative point clouds subjected to distinct distortion types: *biplane* with octree-based compression, *sarah* with trisoup-based compression, *flowerpot* with Gaussian noise, and *bag* with video-based compression. We then compared the subjective MOS with the predicted scores from the multi-scale feature-based TCDM, the learning-based FRSVR, and our proposed MS-ISSM.

The visual analysis shows that MS-ISSM accurately captures steady quality drops as distortion levels increase. For example, in *biplane* with octree-based compression, our method

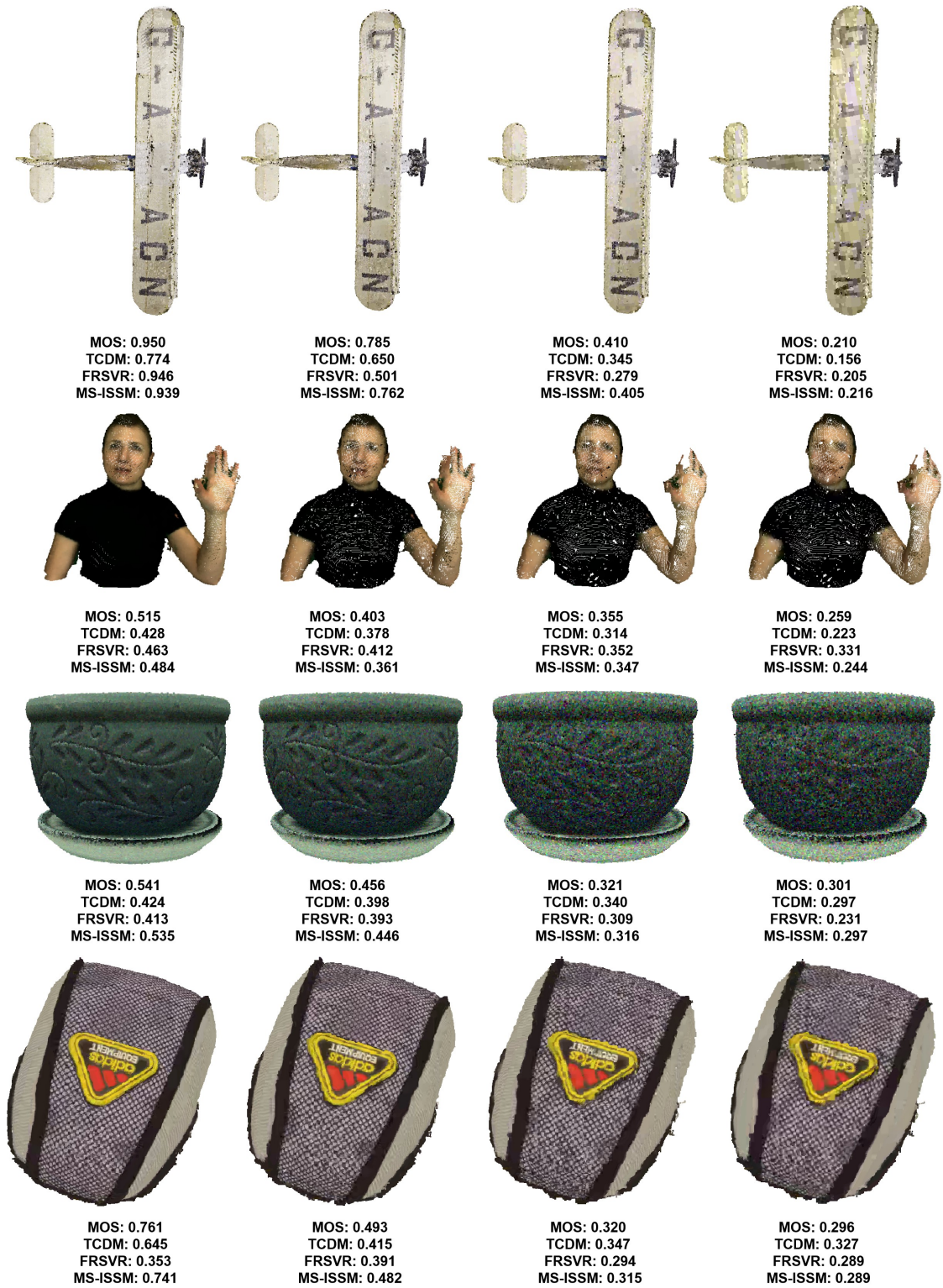


Fig. 6. Qualitative visual comparisons of distorted point clouds and their objective quality scores. From top to bottom, the models are subjected to octree-based compression (*biplane*), trisoup-based compression (*sarah*), Gaussian noise (*flowerpot*), and video compression (*bag*), with distortion severity increasing from left to right. The scores below each model represent the subjective MOS, predictions from two SOTA methods (TCDM and FRSVR), and our proposed MS-ISSM.

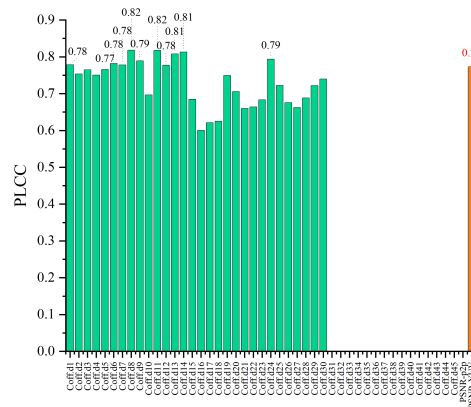
tracks the MOS drop from 0.950 to 0.210 by predicting scores from 0.939 to 0.216, which avoids the consistent underestimation of TCDM and the excessive penalties of FRSVR at medium distortion levels. Furthermore, MS-ISSM is robust to noise, as seen in *flowerpot* with Gaussian noise where TCDM and FRSVR give excessively low scores to small point shifts. In contrast, MS-ISSM uses continuous RBF functions to smooth out these small errors, staying consistent with the HVS. Additionally, in *bag* with video-based compression, FRSVR incorrectly gives a low score of 0.353 to a high-quality model with an MOS of 0.761, causing an incorrect quality ranking. Meanwhile, MS-ISSM correctly tracks the actual quality drop from 0.741 to 0.289. Overall, this visual analysis confirms that MS-ISSM aligns well with human visual perception.

E. Sensitivity Analysis

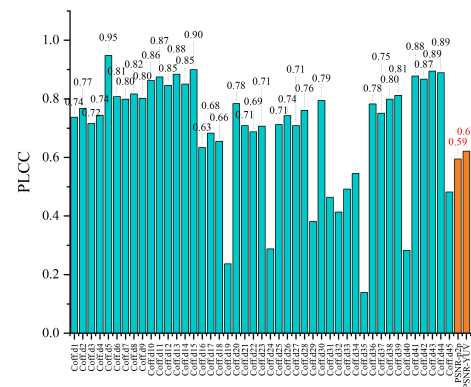
We conducted a sensitivity analysis using the color noise (CN) and geometry noise (GN) subsets from the SJTU dataset to evaluate whether the differences in implicit function coefficients well reflect perceptual distortion. The SJTU dataset defines CN as photometric noise applied to the RGB attributes of randomly selected points. Specifically, the noise is injected into 10%, 30%, 40%, 50%, 60%, and 70% of the points, with corresponding intensity limits set to 10, 30, 40, 50, 60, and 70. GN applies a random Gaussian distributed geometric shift to all points. These shifts are bounded within 0.05%, 0.1%, 0.2%, 0.5%, 0.7%, and 1.2% of the bounding box. We computed the difference in the implicit function coefficient (45-dimensional) for the original and distorted point cloud respectively, and evaluated their correlation in PLCC with the perceptual quality measured in subjective MOS. The results are then compared with traditional point-to-point metrics (PSNR-p2p and PSNR-YUV) on the above subsets.

As shown in Fig. 7, the quantitative results demonstrate that the RBF coefficient differences exhibit a strong correlation with MOS not only at their peak values but across the broader 45-dimensional feature distribution. Under CN, our features achieve a maximum correlation of 0.82, with 11 out of the 30 color-related dimensions explicitly outperforming the traditional PSNR-YUV metric at 0.77, while PSNR-p2p is inherently inapplicable to pure color distortions. Under GN, the coefficients demonstrate even stronger sensitivity with a maximum correlation of 0.95. Furthermore, this superiority is widely distributed across the feature space under GN, where 8 out of the 15 geometry-related dimensions surpass PSNR-p2p at 0.59, and 27 out of the 30 color-related dimensions exceed PSNR-YUV at 0.62. These findings empirically validate that implicit coefficients capture perceptual degradation much more reliably and comprehensively than discrete point matching.

Moreover, to better interpret the superiority of coefficient-space difference, we analyzed *soldier* subjected to two different types of distortions: noise and downsampling. As shown in Fig. 8, we compare the predicted normalized quality scores of PSNR-YUV and our MS-ISSM against the subjective MOS. Because the unstructured nature of point clouds leads to local point coordinate shifts in both scenarios, the traditional



(a) CN



(b) GN

Fig. 7. Sensitivity analysis of the RBF coefficient differences.

point-to-point metric (PSNR-YUV) fails to distinguish their actual perceptual differences, producing almost identical quality scores of 0.61 and 0.59 for downsampling and noise, respectively. In contrast, human vision is relatively tolerant to uniform downsampling with a high MOS of 0.77, but highly sensitive to noise-induced degradation with a low MOS of 0.42. Our MS-ISSM effectively captures this perceptual discrepancy, predicting a high quality score of 0.69 for downsampling and appropriately penalizing the noise distortion with a low score of 0.36. Ultimately, the quality predictions of MS-ISSM align consistently with human visual perception.

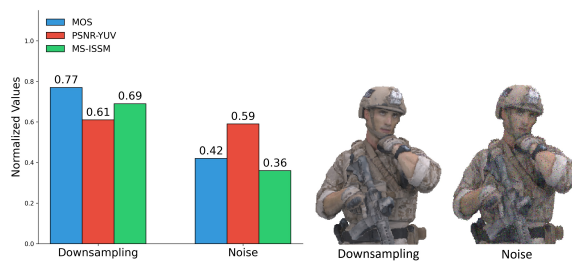


Fig. 8. Coefficient-space difference vs. Point-space error.

F. Complexity Analysis

We compare the average running times across four datasets on an Intel Core i7-8809G CPU @3.10GHz. As shown in Fig. 9, our method achieves superior efficiency, surpassed only by FRSVR. The efficiency of MS-ISSM comes from replacing global topological comparisons with local matrix operations. When the original point cloud has N_O points, the sampled reference point set has N_R points where $N_R \ll N_O$, and the local neighborhood size is set to 30. The algorithm processes the data in several steps. First, iterating points to build multi-scale voxel representations takes $\mathcal{O}(N_O)$ time. Next, building a KD-Tree for spatial partitioning requires $\mathcal{O}(N_O \log N_O)$ operations, and finding nearest neighbors for the N_R reference points takes $\mathcal{O}(N_R \log N_O)$ time. For the extraction of curvature features, calculating the local surface variations involves secondary constant-sized neighborhood searches and matrix decompositions within each patch, which securely bounds to an additional $\mathcal{O}(N_R \log N_O)$ time. Subsequently, solving constant-sized linear systems for local RBF fitting adds $\mathcal{O}(N_R)$ time, while processing feature vectors via the ResGrouped-MLP takes $\mathcal{O}(1)$ time. As summarized in Table V, the overall complexity is dominated by space partitioning and neighbor search. Since these operations are performed on both the original and distorted point clouds, the total time doubles but remains bounded by $\mathcal{O}(N_O \log N_O)$. Graph-based metrics such as GraphSIM and MS-GraphSIM require graph construction or spectral decomposition, while MS-PSSIM and PointPCA are burdened by high-dimensional multi-scale processing in the point space. In contrast, MS-ISSM avoids global topology reconstruction; by restricting complex matrix calculations to highly downsampled reference points, it ensures the linearithmic efficiency shown in Fig. 9. Although simple single-scale metrics like p2p remain computationally light, our method offers a better trade-off between processing speed and multi-scale performance, making it highly suitable for large-scale PCQA.

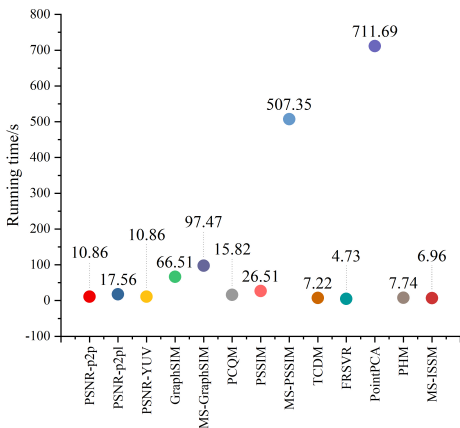


Fig. 9. Time complexity of PCQA methods on four datasets.

G. Ablation Studies

To comprehensively validate the effectiveness of the proposed MS-ISSM framework, we conducted extensive ablation

TABLE V
COMPLEXITY ANALYSIS OF THE PROPOSED MS-ISSM.

Processing Stage	Complexity
multi-scale voxelization	$\mathcal{O}(N_O)$
curvature extraction	$\mathcal{O}(N_R \log N_O)$
space partitioning	$\mathcal{O}(N_O \log N_O)$
KNN search	$\mathcal{O}(N_R \log N_O)$
RBF implicit fitting	$\mathcal{O}(N_R)$
quality regression	$\mathcal{O}(1)$
overall complexity	$\mathcal{O}(N_O \log N_O)$

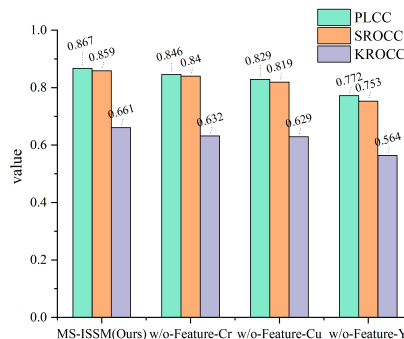


Fig. 10. Performance comparison among different feature types.

studies. These experiments are designed to investigate the contribution of four key aspects: the multi-modal implicit features, the multi-scale strategy, the specific architectural components of the ResGrouped-MLP network, and the key hyperparameters of MS-ISSM. The results are analyzed on the WPC dataset to ensure statistical reliability.

• Impact of Multi-modal Implicit Features

We first investigate the impact of different basis feature functions by evaluating the performance of MS-ISSM when removing single feature types: w/o luma, chroma, or curvature. As illustrated in Fig. 10, while the incomplete models can still provide reasonable quality estimations, omitting any specific feature, particularly luma, exhibits limitations in capturing the full spectrum of perceptual distortions. For instance, geometry distortions are less perceptible when structural features are ablated, and vice versa for color. The complete fusion of multi-modal features yields superior robustness, confirming that combining geometry and color attributes is essential for aligning with the HVS.

• Impact of Multi-scale Strategy

To verify the necessity of the multi-scale hierarchy, we evaluated the performance by ablating individual spatial scales: w/o High, Medium, or Low. As reported in Table VI, although models missing a single scale still achieve decent correlations, their performance fluctuates across different datasets due to varying point cloud densities and content characteristics. For example, omitting the High scale results in a more significant performance drop on datasets with fine textures, while removing the Low scale more severely impairs the evaluation of global structural distortions. By integrating all

three scales, MS-ISSM effectively aggregates local details and global topology, achieving consistent and optimal performance across diverse datasets.

TABLE VI
THE PERFORMANCE COMPARISON OF DIFFERENT SCALES.

Dataset	Scale	PLCC	SROCC	KROCC	RMSE
WPC	MS-ISSM (Ours)	0.867	0.859	0.661	11.618
	w/o-Scale-H	0.846	0.832	0.642	12.227
	w/o-Scale-L	0.833	0.827	0.636	12.674
	w/o-Scale-M	0.849	0.839	0.650	12.098

- Impact of ResGrouped-MLP Architecture

Finally, to justify the design rationale of our regression network, we conducted an ablation study by removing or replacing key modules in the ResGrouped-MLP. The comparison results are summarized in Table VIII. To evaluate the impact of the Log-Modulus transformation, we removed the Log-Modulus preprocessing and used standard Z-score normalization directly on the raw coefficients. As shown in Table VIII, this resulted in a performance drop, with SROCC decreasing by 0.015. This confirms that the raw statistical features follow a heavy-tailed distribution, and the proposed Log-Modulus transformation effectively suppresses outliers, enabling the network to learn more robust feature representations. To validate the "Split-Transform-Merge" strategy, we replaced the grouped encoders with a standard MLP that concatenates all multi-scale features at the input stage. The results show that the grouped strategy outperforms early concatenation by 0.007 in PLCC. This suggests that processing luma, chroma, and curvature features independently in the early layers prevents information interference, allowing the network to capture distinct distortion patterns for each channel. We also removed the scale-wise channel attention blocks to assess their contribution. The subsequent decline in performance indicates that the attention mechanism plays a crucial role in allowing the model to adaptively recalibrate the importance of different channels, thereby better mimicking the varying sensitivities of the HVS. In summary, each component of the MS-ISSM, from implicit feature extraction to the hierarchical regression network, makes a significant contribution to the final prediction accuracy and robustness.

- Impact of Key Hyperparameters

We conducted experiments to evaluate the impact of the number of RBF neighbors, multi-scale voxel sizes, the attention bottleneck ratio, and the reference points sampling size. We evaluated these variants on the WPC dataset to ensure reliability, with results summarized in Table VIII. The underlined values denote our chosen configurations.

TABLE VII
ABLATION STUDY OF THE PROPOSED RESGROUPED-MLP ARCHITECTURE ON THE WPC DATASET.

Model Variant	PLCC	SROCC	KROCC	RMSE
MS-ISSM (Ours)	0.867	0.859	0.661	11.618
w/o Log-Modulus	0.855	0.844	0.657	11.878
w/o Grouped Encoders	0.860	0.848	0.662	11.691
w/o Attention Block	0.852	0.841	0.652	11.987

TABLE VIII
HYPERPARAMETER ABLATION ON WPC DATASET. THE UNDERLINED VALUES DENOTE OUR CHOSEN CONFIGURATIONS.

Hyperparameter	Configuration	PLCC	SROCC
RBF Neighbors	15	0.839	0.837
	<u>30</u>	0.867	0.859
	50	0.832	0.825
Voxel Sizes	(1.0, 2.0, 4.0)	0.849	0.843
	<u>(2.0, 4.0, 8.0)</u>	0.867	0.859
	(4.0, 8.0, 16.0)	0.819	0.822
Bottleneck Ratio	2	0.853	0.841
	<u>4</u>	0.867	0.859
	8	0.846	0.840
Reference Point Size	64	0.833	0.828
	<u>32</u>	0.867	0.859
	8	0.869	0.860

Regarding the RBF neighbors, we tested values of 15, 30, and 50. A smaller neighborhood of 15 yields a localized receptive field sensitive to isolated noise, while a larger neighborhood of 50 results in over-smoothing that masks fine geometry artifacts and increases computational overhead. Setting the value to 30 balances noise robustness and structural sensitivity. For the multi-scale voxel sizes (H, M, L), we evaluated three different progression ranges: a finer scale of (1.0, 2.0, 4.0), our baseline of (2.0, 4.0, 8.0), and a coarser scale of (4.0, 8.0, 16.0). (1.0, 2.0, 4.0) highlights small details but miss large structural changes. Conversely, (4.0, 8.0, 16.0) downsamples the data too much, losing fine artifacts like color quantization noise.

When analyzing the channel reduction ratio within our attention blocks, we tested values of 2, 4, and 8. A low ratio of 2 retains redundant channel information and increases the risk of overfitting. A high ratio of 8 over-compresses the latent space, causing a loss of semantic interactions between physical attributes including luma, chroma, and curvature.

Finally, we evaluated reference point sampling sizes of 64, 32, and 8. A larger size of 64 leads to insufficient local feature extraction and a noticeable performance drop. A smaller size of 8 yields a marginal performance improvement, but substantially increases the computational burden. Selecting a size of 32 provides the trade-off between computational efficiency and evaluation accuracy. Overall, these empirical validations prove the effectiveness of the architectural choices in MS-ISSM.

H. Generalization Analysis

To validate the generalization capabilities of our methods, we conducted cross-dataset evaluations using three large-scale benchmark datasets. Specifically, we trained our model entirely on the WPC dataset and tested it directly on the ICIP, SJTU and M-PCCD datasets. To strictly prevent data leakage, the zero-mean normalization mapping fitted on the training set was directly applied to the testing sets. Table IX below summarizes the results, where SROCC and PLCC values above 0.82 across distinct data distributions can be observed. It is therefore verified that ResGrouped-MLP learns robust and generalized mappings.

TABLE IX
CROSS-DATASET EVALUATION RESULTS TRAINED ON THE WPC DATASET.

Training	Testing	PLCC	SROCC	KROCC	RMSE
WPC	SJTU	0.840	0.827	0.634	1.298
WPC	M-PCCD	0.895	0.918	0.658	0.560
WPC	ICIP	0.914	0.918	0.753	0.497

VI. CONCLUSION

This paper presents a multi-scale implicit structural similarity (MS-ISSM) method for point cloud quality assessment (PCQA). To avoid the accumulation of matching errors in unstructured point clouds, the method leverages implicit functions to represent multi-scale features and evaluates quality based on differences in their coefficients. A ResGrouped-MLP network is introduced, incorporating a Log-Modulus transformation that stabilizes gradient descent and accelerates convergence. The architecture employs a grouped encoding strategy combined with residual blocks and channel-wise attention, enabling the model to preserve distinct physical semantics of luma, chroma, and geometry while adaptively highlighting the most salient distortions across high, medium, and low scales. Experiments demonstrate that MS-ISSM outperforms existing PCQA metrics on public datasets, providing a reliable and consistent quality evaluation.

REFERENCES

- [1] W. Chen, Q. Jiang, W. Zhou, F. Shao, G. Zhai, and W. Lin, "No-reference point cloud quality assessment via graph convolutional network," *IEEE Trans. Multimedia*, vol. 27, pp. 2489–2502, 2025.
- [2] Y. Jin, Z. Ji, D. Zeng, and X. Zhang, "VWP: An efficient DRL-based autonomous driving model," *IEEE Trans. Multimedia*, vol. 26, pp. 2096–2108, 2024.
- [3] Q. Liu, H. Yuan, J. Hou, R. Hamzaoui, and H. Su, "Model-based joint bit allocation between geometry and color for video-based 3D point cloud compression," *IEEE Trans. Multimedia*, vol. 23, pp. 3278–3291, 2021.
- [4] H. Su, Q. Liu, Y. Liu, H. Yuan, H. Yang, Z. Pan, and Z. Wang, "Bitstream-based perceptual quality assessment of compressed 3D point clouds," *IEEE Trans. Image Process.*, vol. 32, pp. 1815–1828, 2023.
- [5] S. Ren, J. Hou, X. Chen, Y. He, and W. Wang, "Geoudf: Surface reconstruction from 3D point clouds via geometry-guided distance representation," in *Proc. IEEE/CVF Int. Conf. Comput. Vis. (ICCV)*, 2023, pp. 14214–14224.
- [6] S. Ren, J. Hou, X. Chen, H. Xiong, and W. Wang, "DDM: A metric for comparing 3D shapes using directional distance fields," *IEEE Trans. Pattern Anal. Mach. Intell.*, vol. 47, no. 8, pp. 6631–6646, Aug. 2025.
- [7] 3DG, "Common Test Conditions for G-PCC," ISO/IEC JTC1/SC29/WG11 output document w22086, 2022.
- [8] E. M. Torlig, E. Alexiou, T. A. Fonseca, R. L. de Queiroz, and T. Ebrahimi, "A novel methodology for quality assessment of voxelized point clouds," in *Proc. Appl. Digit. Image Process. XLI*, vol. 10752, pp. 174–190, 2018.
- [9] E. Alexiou and T. Ebrahimi, "Exploiting user interactivity in quality assessment of point cloud imaging," in *Proc. 11th Int. Conf. Qual. Multimedia Exper. (QoMEX)*, Berlin, Germany, 2019, pp. 1–6.
- [10] Q. Yang, H. Chen, Z. Ma, Y. Xu, R. Tang, and J. Sun, "Predicting the perceptual quality of point cloud: A 3D-to-2D projection-based exploration," *IEEE Trans. Multimedia*, vol. 23, pp. 3877–3891, 2021.
- [11] W. Chen, Q. Jiang, W. Zhou, L. Xu, and W. Lin, "Dynamic hypergraph convolutional network for no-reference point cloud quality assessment," *IEEE Trans. Circuits Syst. Video Technol.*, vol. 34, no. 10, pp. 10479–10493, 2024.
- [12] Q. Liu *et al.*, "PQA-Net: Deep no reference point cloud quality assessment via multi-view projection," *IEEE Trans. Circuits Syst. Video Technol.*, vol. 31, no. 12, pp. 4645–4660, 2021.
- [13] D. Tian, H. Ochimizu, C. Feng, R. Cohen, and A. Vetro, "Geometric distortion metrics for point cloud compression," in *Proc. IEEE Int. Conf. Image Process. (ICIP)*, Beijing, China, 2017, pp. 3460–3464.
- [14] G. Meynet, Y. Nehmé, J. Digne, and G. Lavoué, "PCQM: A full-reference quality metric for colored 3D point clouds," in *Proc. 12th Int. Conf. Qual. Multimedia Exper. (QoMEX)*, Athlone, Ireland, 2020, pp. 1–6.
- [15] A. Javaheri, C. Brites, F. Pereira, and J. Ascenso, "Point cloud rendering after coding: Impacts on subjective and objective quality," *IEEE Trans. Multimedia*, vol. 23, pp. 4049–4064, 2021.
- [16] M. P. Sampat, Z. Wang, S. Gupta, A. C. Bovik, and M. K. Markey, "Complex wavelet structural similarity: A new image similarity index," *IEEE Trans. Image Process.*, vol. 18, no. 11, pp. 2385–2401, Nov. 2009.
- [17] Z. Chen, S. Wan, S. Ren, F. Yang, M. Yu, and J. Hou, "RBFIM: Perceptual quality assessment for compressed point clouds using radial basis function interpolation," *IEEE Trans. Multimedia*, vol. 27, pp. 8579–8591, 2025.
- [18] A. Javaheri, C. Brites, F. Pereira, and J. Ascenso, "Mahalanobis based point to distribution metric for point cloud geometry quality evaluation," *IEEE Signal Process. Lett.*, vol. 27, pp. 1350–1354, 2020.
- [19] P. Cignoni, C. Rocchini, and R. Scopigno, "Metro: Measuring error on simplified surfaces," in *Comput. Graph. Forum*, vol. 17, no. 2. Oxford, UK and Boston, USA: Blackwell Publishers, 1998.
- [20] E. Alexiou and T. Ebrahimi, "Point cloud quality assessment metric based on angular similarity," in *Proc. IEEE Int. Conf. Multimedia Expo (ICME)*, San Diego, CA, USA, 2018, pp. 1–6.
- [21] G. Meynet, J. Digne, and G. Lavoué, "PC-MSDM: A quality metric for 3D point clouds," in *Proc. 11th Int. Conf. Qual. Multimedia Exper. (QoMEX)*, Berlin, Germany, 2019, pp. 1–3.
- [22] E. Alexiou and T. Ebrahimi, "Exploiting user interactivity in quality assessment of point cloud imaging," in *Proc. 11th Int. Conf. Qual. Multimedia Exper. (QoMEX)*, Berlin, Germany, 2019, pp. 1–6.
- [23] Y. Zhang, K. Ding, N. Li, H. Wang, X. Huang, and C.-C. J. Kuo, "Perceptually weighted rate distortion optimization for video-based point cloud compression," *IEEE Trans. Image Process.*, vol. 32, pp. 5933–5947, 2023.
- [24] I. Viola, S. Subramanyam, and P. Cesar, "A color-based objective quality metric for point cloud contents," in *Proc. 12th Int. Conf. Qual. Multimedia Exper. (QoMEX)*, Athlone, Ireland, 2020, pp. 1–6.
- [25] Q. Yang, Z. Ma, Y. Xu, Z. Li, and J. Sun, "Inferring point cloud quality via graph similarity," *IEEE Trans. Pattern Anal. Mach. Intell.*, vol. 44, no. 6, pp. 3015–3029, 2022.
- [26] Y. Zhang, Q. Yang, and Y. Xu, "MS-GraphSIM: Inferring point cloud quality via multiscale graph similarity," in *Proc. 29th ACM Int. Conf. Multimedia*, 2021, pp. 1230–1238.
- [27] E. Alexiou and T. Ebrahimi, "Towards a point cloud structural similarity metric," in *Proc. IEEE Int. Conf. Multimedia Expo Workshops (ICMEW)*, London, UK, 2020, pp. 1–6.
- [28] Q. Yang, Y. Zhang, S. Chen, Y. Xu, J. Sun, and Z. Ma, "MPED: Quantifying point cloud distortion based on multiscale potential energy discrepancy," *IEEE Trans. Pattern Anal. Mach. Intell.*, vol. 45, no. 5, pp. 6037–6054, 2023.
- [29] Y. Zhang, Q. Yang, Y. Zhou, X. Xu, L. Yang, and Y. Xu, "TCDM: Transformational complexity based distortion metric for perceptual point cloud quality assessment," *IEEE Trans. Vis. Comput. Graphics*, vol. 30, no. 10, pp. 6707–6724, 2024.
- [30] Y. Zhang, Q. Yang, Y. Xu, and S. Liu, "Perception-guided quality metric of 3D point clouds using hybrid strategy," *IEEE Trans. Image Process.*, vol. 33, pp. 5755–5770, 2024.
- [31] D. Lazzarotto and T. Ebrahimi, "Towards a multiscale point cloud structural similarity metric," in *Proc. IEEE 25th Int. Workshop Multimedia Signal Process. (MMSp)*, Poitiers, France, 2023, pp. 1–6.
- [32] A. Chetouani, M. Quach, G. Valenzise, and F. Dufaux, "Convolutional neural network for 3D point cloud quality assessment with reference," in *Proc. IEEE 23rd Int. Workshop Multimedia Signal Process. (MMSp)*, Tampere, Finland, 2021, pp. 1–6.
- [33] M. Tliba, A. Chetouani, G. Valenzise, and F. Dufaux, "PCQA-Graphpoint: Efficient deep-based graph metric for point cloud quality assessment," in *Proc. IEEE Int. Conf. Acoust., Speech, Signal Process. (ICASSP)*, Rhodes Island, Greece, 2023, pp. 1–5.
- [34] E. Alexiou, X. Zhou, I. Viola, and P. Cesar, "PointPCA: Point cloud objective quality assessment using PCA-based descriptors," in *EURASIP J. Image Video Process.*, vol. 20, 2024.
- [35] R. Watanabe, K. Nonaka, E. Pavez, T. Kobayashi, and A. Ortega, "Full-reference point cloud quality assessment using spectral graph wavelets," in *Proc. IEEE Int. Conf. Image Process. (ICIP)*, Abu Dhabi, United Arab Emirates, 2024, pp. 3313–3319.

- [36] R. Watanabe, S. N. Sridhara, H. Hong, E. Pavez, K. Nonaka, T. Kobayashi, and A. Ortega, "Full-reference point cloud quality assessment using support vector regression," *Signal Process., Image Commun.*, vol. 131, p. 117239, 2025.
- [37] M. Cui, Y. Zhang, C. Fan, R. Hamzaoui, and Q. Li, "Colored point cloud quality assessment using complementary features in 3D and 2D spaces," *IEEE Trans. Multimedia*, vol. 26, pp. 11111–11125, 2024.
- [38] J. Wang, W. Gao, and G. Li, "Applying collaborative adversarial learning to blind point cloud quality measurement," *IEEE Trans. Instrum. Meas.*, vol. 72, pp. 1–15, 2023.
- [39] A. Javaheri, C. Brites, F. Pereira, and J. Ascenso, "Joint geometry and color projection-based point cloud quality metric," *IEEE Access*, vol. 10, pp. 90481–90497, 2022.
- [40] Q. Liu, H. Su, Z. Duanmu, W. Liu, and Z. Wang, "Perceptual quality assessment of colored 3D point clouds," *IEEE Trans. Vis. Comput. Graphics*, vol. 29, no. 8, pp. 3642–3655, 2023.
- [41] X. G. Freitas, R. Diniz, and M. C. Farias, "Point cloud quality assessment: Unifying projection, geometry, and texture similarity," *Vis. Comput.*, vol. 39, pp. 1907–1914, 2023.
- [42] M. D. Buhmann, "Radial basis functions," *Acta Numerica*, vol. 9, pp. 1–38, 2000.
- [43] VQEG, "Final report from the video quality experts group on the validation of objective models of video quality assessment," [Online]. Available: <http://www.its.bldrdoc.gov/vqeg/vqeg-home.aspx>.
- [44] E. Alexiou, I. Viola, T. M. Borges, T. A. Fonseca, R. L. De Queiroz, and T. Ebrahimi, "A comprehensive study of the rate-distortion performance in MPEG point cloud compression," *APSIPA Trans. Signal Inf. Process.*, vol. 8, 2019.
- [45] S. Perry *et al.*, "Quality evaluation of static point clouds encoded using MPEG codecs," in *Proc. IEEE Int. Conf. Image Process. (ICIP)*, 2020, pp. 3428–3432.